

# Oxygen Vacancies Enhanced NiCo<sub>2</sub>O<sub>4</sub> Nanoarrays on Carbon Cloth as Cathode for Flexible Supercapacitors with Excellent Cycling Stability

Dongming Cai,<sup>[a]</sup> Qinghe Cao,<sup>[b]</sup> Junjie Du,<sup>[b]</sup> Yang Liu,<sup>[b]</sup> Fan Bu,<sup>[b]</sup> Yonghui Yan,<sup>[b]</sup> Xinhuan Lu,<sup>[a]</sup> Qinghua Xia,<sup>[a]</sup> Dan Zhou,\*<sup>[a]</sup> and Yongde Xia\*<sup>[c]</sup>

Defect engineering such as oxygen vacancy in heterostructured electrode materials has emerged as a promising strategy to improve material performance in energy storage and conversion fields. The most common methods to introduce oxygen vacancies in energy materials usually involve high temperature treatment or strong reducing agents. In this work, we adopted a mild solvothermal treatment method to introduce oxygen vacancies into NiCo<sub>2</sub>O<sub>4</sub> (Vo-NiCo<sub>2</sub>O<sub>4</sub>) nanoarrays. Owing to the increased oxygen vacancies and the improved surface area, the as-prepared Vo-NiCo<sub>2</sub>O<sub>4</sub> on carbon cloth (Vo-NiCo<sub>2</sub>O<sub>4</sub>@CC) shows a high specific capacitance of 1389 mF cm<sup>-2</sup> under the current density of 0.5 mA cm<sup>-2</sup>, and a remarkable capacitance

retention of 93.8% after 10000 cycles when used as cathode for supercapacitor. Moreover, an aqueous asymmetric supercapacitor was assembled using Vo-NiCo<sub>2</sub>O<sub>4</sub>@CC as cathode and AC@CC as anode and this device delivers a high energy density of 43.6 Wh kg<sup>-1</sup> at a power density of 281 W kg<sup>-1</sup>. In addition, the as-assembled quasi-solid state asymmetric supercapacitor exhibits excellent mechanical flexibility and functions well while being bent at large angles or being twisted. This work offers a facile, cost-effective and practical available approach to finely tune the surface property of electrode materials towards flexible energy storage devices for wearable applications.

## Introduction

With the fast increased energy demand and the rapid consumption of fossil fuel-based energy resources, significant attention has been paid to exploit green and sustainable energy resources. Among a variety of energy storage systems, electrochemical energy system has attracted remarkable research interest due to its great potential in a wide range of practical applications, especially in the portable electronic products that are indispensable in contemporary life and can be powered by electrochemical energy storage technologies.<sup>[1–3]</sup> Different from the commercialized batteries, supercapacitors (SCs) normally exhibit high power density and fast charge-discharge as well as comparable rate performance. Moreover, many wearable products such as wearable sensors,

portable communication devices, smart textiles and medical actuators, are urged to be fabricated and powered by SCs, to meet the increased demands for smart life.<sup>[4–6]</sup> However, the current commercial SCs present some challenges for their utilizations in flexible electronics due to the use of organic electrolytes which inevitably bring some safety concerns.<sup>[7]</sup> To avoid the usage of flammable and corrosive organic electrolytes, the use of aqueous solution of electrolytes is an alternative choice. However, the limited voltage of water splitting and the narrower working voltage window, often lead to lower energy density of aqueous SCs. Actually, many reported energy densities of aqueous SCs are in the range of 0.01–0.1 mWh cm<sup>-2</sup>.<sup>[8,9]</sup> Therefore, developing flexible aqueous SCs with high energy density is sought-after and highly desirable.

Many works have been carried out to realize the high energy density of SCs, among which pseudo-capacitive materials, especially transition metal oxides (TMOs) are widely investigated since they involve Faradaic process, rather than purely electrostatic process, which thus dramatically increase the capacitance as well as the energy density of supercapacitors.<sup>[7,10,11]</sup> In addition, the natural abundance, low cost and environmental benignity of most TMOs also make them ideal candidates for energy storage applications.<sup>[12–15]</sup> In particular, many efforts have been devoted to binary transition metal oxides, such as NiCo<sub>2</sub>O<sub>4</sub>, due to their high reversible redox capability, the good electrochemical conductivity as well as the multivalences of transition metal elements.<sup>[16–19]</sup> However, the limited surface area of NiCo<sub>2</sub>O<sub>4</sub> frequently hinders its fully utilization as an active pseudo-capacitive material and leads to dissatisfied electrochemical performance. Therefore,

[a] D. Cai, Dr. X. Lu, Prof. Q. Xia, Prof. D. Zhou  
Hubei Collaborative Innovation Center for Advanced Organic Chemical Materials

Ministry-of-Education Key Laboratory for the Synthesis and Application of Organic Functional Molecules  
Hubei University  
Wuhan, 430062, China

E-mail: d.zhou@hubu.edu.cn

[b] Q. Cao, J. Du, Y. Liu, F. Bu, Y. Yan  
Institute of Flexible Electronics  
Northwestern Polytechnical University  
Xi'an, 710129, China

[c] Dr. Y. Xia  
College of Engineering, Mathematics and Physical Sciences  
University of Exeter  
Exeter, EX4 4QF, United Kingdom  
E-mail: Y.Xia@exeter.ac.uk

 Supporting information for this article is available on the WWW under  
<https://doi.org/10.1002/batt.202100344>

some strategies have been developed to enhance the performance of pristine  $\text{NiCo}_2\text{O}_4$ . For example, Yan et al. used a chemical reduction method to introduce moderate oxygen vacancies in  $\text{NiCo}_2\text{O}_4$  and the resulting material exhibited enhanced conductivity and capacitance after the chemical treatment by  $\text{NaBH}_4$  solution.<sup>[20]</sup> Wen et al. reported an integrated electrode of  $\text{MoS}_2/\text{NiCo}_2\text{O}_4$  by using  $\text{NiCo}_2\text{O}_4$  nanoarrays as skeleton to load active material  $\text{MoS}_2$ .<sup>[21]</sup> Moreover, Ouyang et al. decorated  $\text{NiCo}_2\text{O}_4$  with ultrathin  $\text{NiO}$  nanosheets and constructed a hierarchical electrode of  $\text{NiO}/\text{NiCo}_2\text{O}_4$  to achieve high capacitance and good cycling stability.<sup>[17]</sup> However, the above mentioned approaches either are destructive to the macrostructure of crystalline  $\text{NiCo}_2\text{O}_4$ , which alters the nature of the electrode materials, or the material process procedures are too complicated.<sup>[22]</sup> Hence, developing facile and cost-effective strategies to efficiently improve the capacitance of  $\text{NiCo}_2\text{O}_4$  is still of great challenge.

Vacancy engineering has been proven to be an efficient approach to enhance the redox reaction rate and improve the adsorption ability of  $\text{OH}^-$  on the surface of materials. In this work, we develop a simple and efficient method to introduce oxygen vacancies to enhance the capacitance of  $\text{NiCo}_2\text{O}_4$  without using of risky reductive agents. The pristine  $\text{NiCo}_2\text{O}_4$  is facilely modified by a mild solvothermal treatment method with the reducibility of ethylene glycol in  $\text{NaOH}$  solution. The modified  $\text{NiCo}_2\text{O}_4$  and pristine  $\text{NiCo}_2\text{O}_4$  are fully characterized by various techniques including X-ray photoelectron spectroscopy, gas sorption analysis as well as electron paramagnetic resonance, and their applications as electrode materials in SCs were evaluated. It was found that the solvothermal treated  $\text{NiCo}_2\text{O}_4$  shows remarkably enhanced specific capacitance as well as superior cycling performance, which is ascribed to its high oxygen defects and a lower valence of Ni and Co species, as well as a much higher specific surface area. This mild reduction strategy may pave a new way for the construction of advanced defect-rich materials for energy storage applications.

## Results and Discussion

### Structure characterization of electrode materials

The preparation procedure of  $\text{Vo-NiCo}_2\text{O}_4@\text{CC}$  is schematically shown in Figure 1. Through a facile hydrothermal process, the  $\text{NiCo-LDH}$  was successfully grown on the CC, as confirmed by the XRD displayed in Figure S1(a). Then  $\text{NiCo}_2\text{O}_4@\text{CC}$  was obtained by the calcination of  $\text{NiCo-LDH}@CC$  at  $300^\circ\text{C}$  in air. Followed by a heat treatment of  $\text{NiCo}_2\text{O}_4@\text{CC}$  in ethylene glycol alkaline solution at  $120^\circ\text{C}$  for different duration,  $\text{Vo-NiCo}_2\text{O}_4@\text{CC}$  was finally obtained. During the last process, ethylene glycol plays the role as mild reducing agent and  $\text{NaOH}$  provides an alkaline medium. It is anticipated that after this mild ethylene glycol alkaline solution treatment, oxygen vacancies can be readily introduced into the structure of these  $\text{Vo-NiCo}_2\text{O}_4@\text{CC}$  samples. A schematic illustration of oxygen vacancies formation of  $\text{Vo-NiCo}_2\text{O}_4@\text{CC}$  from the  $\text{NiCo}_2\text{O}_4@\text{CC}$  is demonstrated in Figure S2.

Figures 2(a) and S1(b and c) show the morphology of  $\text{NiCo-LDH}@CC$ . From these SEM images, it is observed that  $\text{NiCo-LDH}$  nanoneedles are very smooth and uniformly distributed on the carbon cloth (CC) fiber. After calcined at  $300^\circ\text{C}$  in air, the  $\text{NiCo-LDH}$  nanoneedle arrays transform to  $\text{NiCo}_2\text{O}_4$ , without obviously alteration of its original morphology, as demonstrated by the SEM images in Figure 2(b) as well as Figure S3(a and b). These  $\text{NiCo}_2\text{O}_4$  nanoneedles are generally vertical aligned on carbon cloth which is beneficial to the fully contact of active materials with electrolyte and realizing fast charge transportation during the electrochemical process.<sup>[23]</sup> Through the mild solvothermal treatment,  $\text{Vo-NiCo}_2\text{O}_4@\text{CC}$  sample is obtained. Although the morphology of nanoneedle arrays has largely remained, the surface of  $\text{Vo-NiCo}_2\text{O}_4@\text{CC}$  is fairly rough with wrinkles, the top of the nanoneedles becomes blunt and the nanoneedles actually turn to nanorods with increased diameter (shown in Figure 2c), which is different from the morphology of the pristine  $\text{NiCo}_2\text{O}_4@\text{CC}$  in Figure 2(b). As demonstrated by the SEM images in Figure S3, with increase in the solvothermal process time in ethylene glycol alkaline

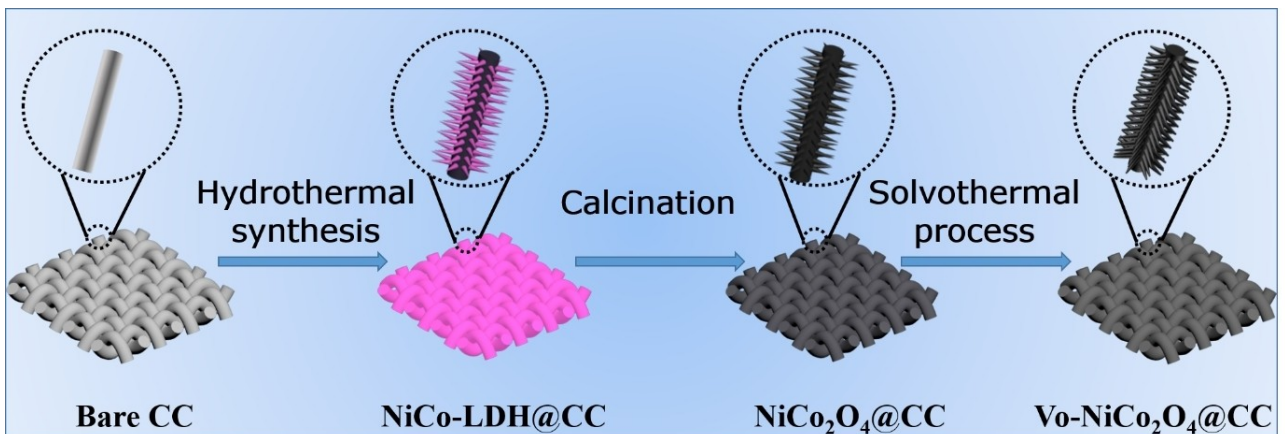
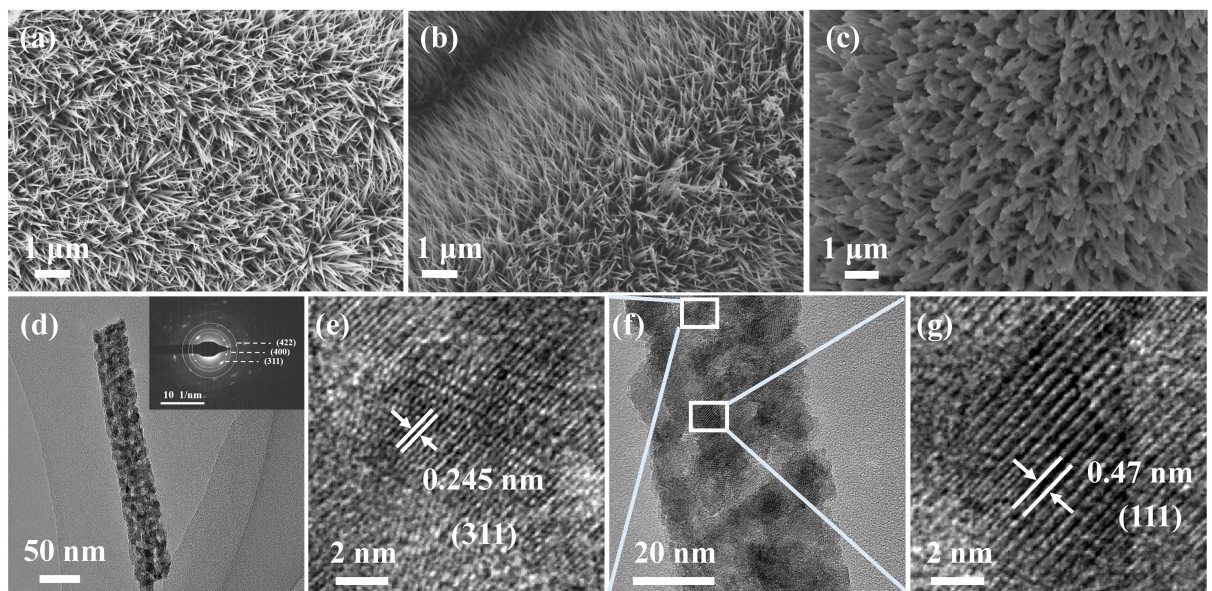


Figure 1. Schematic diagram of the preparation of  $\text{Vo-NiCo}_2\text{O}_4@\text{CC}$ .



**Figure 2.** SEM images of a) NiCo-LDH@CC, b) NiCo<sub>2</sub>O<sub>4</sub>@CC and c) Vo-NiCo<sub>2</sub>O<sub>4</sub>@CC-16h. d–g) TEM images of Vo-NiCo<sub>2</sub>O<sub>4</sub>@CC-16h. The inset in (d) is SAED pattern.

solution, rough surface and porous structure were formed during the solvothermal reduction process, possibly due to the introduction of increased defects into the Vo-NiCo<sub>2</sub>O<sub>4</sub>@CC samples. Actually, the morphologies of Vo-NiCo<sub>2</sub>O<sub>4</sub>@CC samples obtained at different solvothermal process time are different from that of pristine NiCo<sub>2</sub>O<sub>4</sub>@CC, which clearly reflects the remarkable effect of reduction treatment duration in the ethylene glycol alkaline solution on the morphology evolution of the Vo-NiCo<sub>2</sub>O<sub>4</sub>@CC samples. Long solvothermal treatment up to 24 h (Figure S3g and h) may partially damage the morphology of pristine NiCo<sub>2</sub>O<sub>4</sub> due to the overreaction. Moreover, TEM image of the representative Vo-NiCo<sub>2</sub>O<sub>4</sub>@CC-16h in Figure 2(d) confirms the presence of porous structure in the sample. Such type of porous structure benefits to the fast transportation of ions and enables fully contact between the electrolyte and the active materials. The corresponding selected-area electron diffraction (SAED) pattern of the solvothermal processed sample Vo-NiCo<sub>2</sub>O<sub>4</sub>@CC-16h exhibits a series of obvious bright concentric rings as shown in the inset of Figure 2(d), which reveals that the polycrystalline nature of the Vo-NiCo<sub>2</sub>O<sub>4</sub> sample.<sup>[18,24]</sup> The high-resolution TEM (HRTEM) images of representative sample Vo-NiCo<sub>2</sub>O<sub>4</sub>@CC in Figure 2(e–g) show the lattice fringes of 0.245 and 0.47 nm that are in line with the theoretical interplanar spacing of (311) and (111) planes of spinel NiCo<sub>2</sub>O<sub>4</sub> (JCPDS card No. 20-0781, cubic phase) respectively, which further indicates that the solvothermal treatment does not change the phase of Vo-NiCo<sub>2</sub>O<sub>4</sub>@CC. The energy-dispersive X-ray spectroscopy (EDS) element mapping images suggest that all the elements Ni, Co, and O are homogeneously distributed in the representative Vo-NiCo<sub>2</sub>O<sub>4</sub>@CC sample (Figure S4).

To identify the crystalline phase of NiCo<sub>2</sub>O<sub>4</sub>@CC samples, powder XRD patterns of the samples are measured, and the results are presented in Figure 3(a). In these XRD patterns,

except the obvious diffraction peak located at  $2\theta$  of  $26^\circ$  is ascribed to the carbon cloth substrate, all the other diffraction peaks of the pristine and solvothermal treated NiCo<sub>2</sub>O<sub>4</sub>@CC samples are exclusively assigned to NiCo<sub>2</sub>O<sub>4</sub> (JCPDS No. 20-0781) and no peaks from any impurities are detected, indicating that pure NiCo<sub>2</sub>O<sub>4</sub> crystals are exclusively formed in these samples.<sup>[25–27]</sup> These results are also well consistent with the HRTEM analyses. Moreover, it is interesting to note that, compared to the pristine NiCo<sub>2</sub>O<sub>4</sub>@CC, the (400) Bragg diffraction peak at  $2\theta$  of  $45^\circ$  for samples Vo-NiCo<sub>2</sub>O<sub>4</sub>@CC gradually shifts to lower  $2\theta$  angles as the solvothermal treatment time increased, indicating the expansion of lattice spacing during the solvothermal treatment process, which may attribute to the introduction of oxygen vacancies in Vo-NiCo<sub>2</sub>O<sub>4</sub>@CC samples.<sup>[28–30]</sup> In addition, the increase of interplanar spacing may facilitate K<sup>+</sup> diffusion in the structure, thus leads to the enhancement of the capacitance of the material.<sup>[31,32]</sup>

N<sub>2</sub> adsorption-desorption isotherms of Vo-NiCo<sub>2</sub>O<sub>4</sub>-xh and pristine NiCo<sub>2</sub>O<sub>4</sub> are measured to investigate textural properties and porosity information of the samples. As shown in Figure 3(b), all the four samples display type-IV isotherms with obvious hysteresis loop in the relative pressure ( $P/P_0$ ) range of 0.6–1.0, which indicates that all NiCo<sub>2</sub>O<sub>4</sub> samples possess a larger amount of mesopores.<sup>[33,34]</sup> Based on BET method, the calculated specific surface area is 82, 105, 124 and 129 m<sup>2</sup> g<sup>-1</sup> for pristine NiCo<sub>2</sub>O<sub>4</sub> and solvothermal treated Vo-NiCo<sub>2</sub>O<sub>4</sub> with different treatment duration of 8, 16 and 24 h respectively. It is worthwhile noting that the specific surface area of the samples increases almost linearly with the solvothermal treatment time up to 16 h; However, as shown in Figure S5(a), when the solvothermal treatment time is prolonged to 24 h, the specific surface area of the resulting Vo-NiCo<sub>2</sub>O<sub>4</sub>-24 h just slightly increases. The pore-size distributions of these four samples

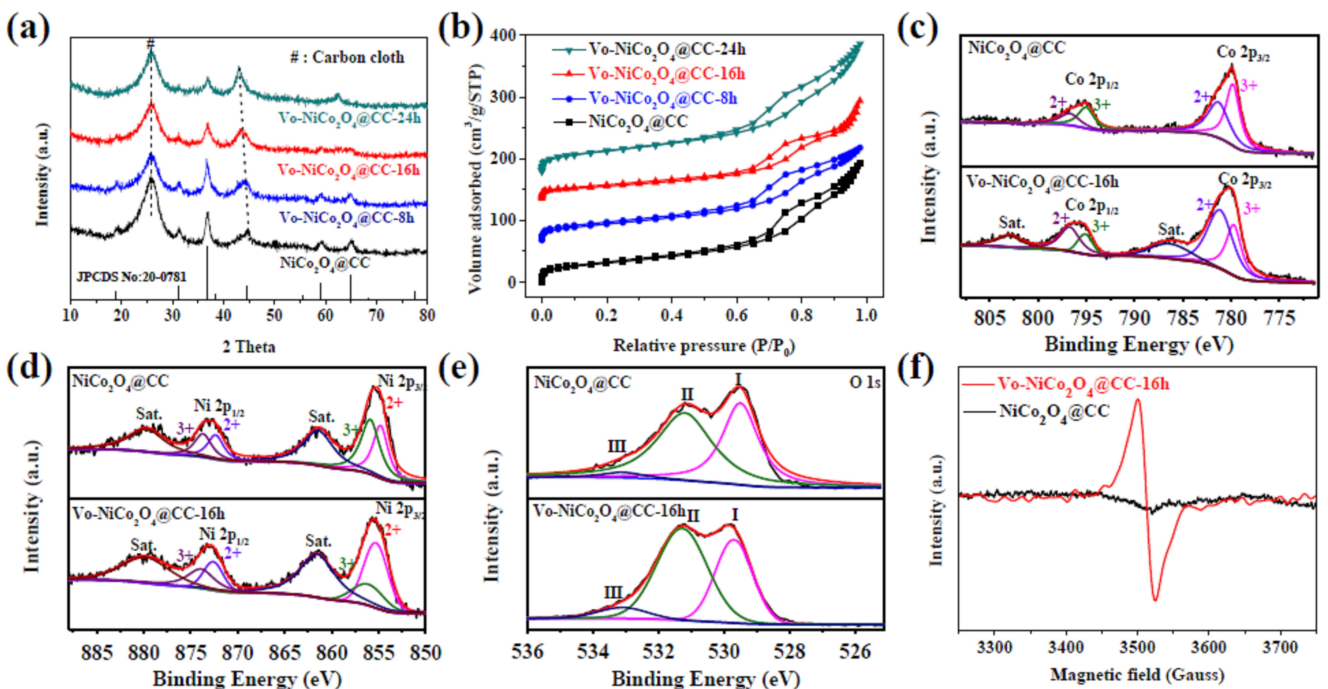


**Figure 3.** a) XRD and b)  $N_2$  adsorption-desorption isotherms of  $Vo\text{-NiCo}_2\text{O}_4\text{@CC-}x\text{h}$  samples ( $x=0, 8, 16, 24$ ) samples; c) Co 2p, d) Ni 2p, e) O 1s XPS spectra and f) EPR spectra of samples  $Vo\text{-NiCo}_2\text{O}_4\text{@CC-16h}$  and  $\text{NiCo}_2\text{O}_4\text{@CC}$ .

were calculated via BJH method based on the adsorption branch of the  $N_2$  isotherms are presented in Figure S5(b). The similar pore size of the four samples implies that this mild solvothermal treatment method is an effective strategy to boost the surface area of the treated samples, but it does not influence remarkably on the pore sizes of  $Vo\text{-NiCo}_2\text{O}_4$  samples.<sup>[22]</sup> Among the four samples,  $Vo\text{-NiCo}_2\text{O}_4\text{@CC-16h}$  presents slightly larger pore size, as shown in Figure S5(c). Samples with high surface area and large pore size offer more accessible active sites, faster electron/ion transfer rates and shorter ions diffusion distance during the electrochemical measurements, which may result in promising high electrochemical performance.

XPS was conducted to identify the chemical status of the elements in pristine  $\text{NiCo}_2\text{O}_4$  and representative  $Vo\text{-NiCo}_2\text{O}_4\text{-16h}$ , which are presented in Figure 3(c-e) and the relative content of different elements including Co, Ni and O derived from XPS analysis of these two samples are summarized in Table S1. The high resolution XPS of Co 2p (Figure 3c) can be split into two spin-orbit doublets and two shakeup satellites (sat.). While the fitted peaks with binding energy located at 779.7 and 795.1 eV are attributed to  $2p_{3/2}$  and  $2p_{1/2}$  of  $\text{Co}^{3+}$  respectively, the peaks located at 781.1 and 796.7 eV are ascribed to  $2p_{3/2}$  and  $2p_{1/2}$  of  $\text{Co}^{2+}$ .<sup>[35]</sup> Compared to  $\text{NiCo}_2\text{O}_4\text{@CC}$ , the fitted XPS of Co 2p of sample  $Vo\text{-NiCo}_2\text{O}_4\text{@CC-16h}$  exhibits two pronounced satellite peaks at 786.3 and 803 eV, which are attributed to  $\text{Co}^{2+}$  oxidation state. These observations indicate that a portion of  $\text{Co}^{2+}$  ions are reduced from  $\text{Co}^{3+}$  through the alkaline solution of ethylene glycol treatment and oxygen vacancies are formed simultaneously, which are well in line with previous reports.<sup>[36-38]</sup> It is noteworthy that the atomic ratio

of  $\text{Co}^{2+}/\text{Co}^{3+}$  of sample  $Vo\text{-NiCo}_2\text{O}_4\text{@CC-16h}$  is 1.79, which is much higher than that of the pristine  $\text{NiCo}_2\text{O}_4\text{@CC}$  (0.83), clearly suggesting the formation of surface oxygen vacancies on  $Vo\text{-NiCo}_2\text{O}_4\text{@CC-16h}$  and those surface oxygen vacancies were balanced by the conversion of  $\text{Co}^{3+}$  to  $\text{Co}^{2+}$ .<sup>[22,28]</sup> Moreover, the high resolution XPS of Ni 2p (Figure 3d) exhibits similar trend as that of Co 2p. The Ni 2p spectra for both the pristine  $\text{NiCo}_2\text{O}_4\text{@CC}$  and  $Vo\text{-NiCo}_2\text{O}_4\text{@CC-16h}$  samples consist of two spin-orbit doublets characteristic of  $\text{Ni}^{2+}$  and  $\text{Ni}^{3+}$  and two shakeup satellite peaks.<sup>[39-41]</sup> As deduced from the area with fitted curve covered of the  $\text{Ni}^{2+}$  and  $\text{Ni}^{3+}$  peaks in the Ni 2p core level spectra, it is obvious that  $Vo\text{-NiCo}_2\text{O}_4\text{@CC-16h}$  is dominated by the lower oxidation state of  $\text{Ni}^{2+}$ , with obvious higher  $\text{Ni}^{2+}/\text{Ni}^{3+}$  ratio in  $Vo\text{-NiCo}_2\text{O}_4\text{@CC-16h}$  than that in pristine  $\text{NiCo}_2\text{O}_4\text{@CC}$ , which can also account for the existence of increased oxygen vacancies in sample  $Vo\text{-NiCo}_2\text{O}_4\text{@CC-16h}$ . For element O, the high resolution XPS of O 1s can be deconvoluted into three peaks (denoted as I, II, III), as shown in Figure 3(e), the peak I located at binding energy of 529.7 eV is ascribed to the interaction of Ni/Co-oxygen bond ( $\text{O}^{2-}$ ), the peak II located at 531.2 eV is the low coordination state of oxygen with high defects, and the higher peak intensity for  $Vo\text{-NiCo}_2\text{O}_4\text{@CC-16h}$  suggests the enrichment of oxygen vacancies was achieved via a mild ethylene glycol alkaline solution treatment.<sup>[22,42-44]</sup> The peak III at 533.1 eV is due to the adsorbed water molecules. To further ratify the formation of oxygen vacancies, electron paramagnetic resonance (EPR) measurements were carried out for the pristine  $\text{NiCo}_2\text{O}_4\text{@CC}$  and representative  $Vo\text{-NiCo}_2\text{O}_4\text{@CC-16h}$  sample. The  $\text{NiCo}_2\text{O}_4\text{@CC}$  showed a negligible EPR signal, but the strong EPR signal corresponding to the electrons trapped on oxygen vacancies

can be observed in the  $\text{Vo-NiCo}_2\text{O}_4@\text{CC-16h}$  sample, suggesting the existence of abundant oxygen vacancies in  $\text{Vo-NiCo}_2\text{O}_4@\text{CC-16h}$ .<sup>[30,43]</sup> Based on the XPS analysis and EPR data, it is clear that after solvothermal treatment, the resulting  $\text{Vo-NiCo}_2\text{O}_4@\text{CC-16h}$  sample possesses abundant formed oxygen vacancies, and lower valance states of Ni and Co. The dominant surface  $\text{Ni}^{2+}/\text{Co}^{2+}$  is of great importance to improve the electrochemical performance of  $\text{Vo-NiCo}_2\text{O}_4@\text{CC-16h}$  sample, since  $\text{Ni}^{3+}/\text{Co}^{3+}$  are basically inactive species for electrochemical reaction.<sup>[45]</sup>

### Electrochemical performance

Electrochemical tests were carried out to evaluate the effect of solvothermal treatment on the electrochemical performance of the modified  $\text{NiCo}_2\text{O}_4$ . As shown in Figure 4(a), the cyclic voltammetry (CV) curves of the representative  $\text{Vo-NiCo}_2\text{O}_4@\text{CC-16h}$  display an obvious pair of redox peaks at various scanning rates, indicating good pseudocapacitive behavior of this sample. Similarly, the galvanostatic charge-discharge (GCD)

curves (Figure 4b) show plateaus in the charge and discharge process evidently, which is in agreement well with the CV results. The other samples exhibit the similar trend and their detailed CV and GCD curves are provided in Figure S6. The comparison of CV curves of  $\text{Vo-NiCo}_2\text{O}_4@\text{CC}$  with solvent thermal treatment of different time are presented in Figure 4(c). The pair of redox peaks are clearly observed for all the  $\text{Vo-NiCo}_2\text{O}_4@\text{CC-xh}$  samples, but the pair of redox peaks for pristine  $\text{NiCo}_2\text{O}_4@\text{CC}$  are not easily visible. Obviously, compared with pristine  $\text{NiCo}_2\text{O}_4@\text{CC}$  at the same scanning rates, the  $\text{Vo-NiCo}_2\text{O}_4@\text{CC}$  samples show much more obvious pairs of redox peaks as well as larger integrated area. In particular, sample  $\text{Vo-NiCo}_2\text{O}_4@\text{CC-16h}$  exhibits the largest integrated area amongst all the studied samples. These results demonstrated that the mild solvothermal treatment of  $\text{NiCo}_2\text{O}_4@\text{CC}$  in ethylene glycol alkaline solution is a facile and effective approach to afford remarkably modified materials like  $\text{Vo-NiCo}_2\text{O}_4@\text{CC-16h}$  with dramatically improved energy storage ability.<sup>[46,47]</sup> This is maybe due to the fact that solvothermal treatment of  $\text{NiCo}_2\text{O}_4@\text{CC}$  in ethylene glycol alkaline solution can readily introduce enhanced oxygen vacancies into the  $\text{Vo-NiCo}_2\text{O}_4@\text{CC}$  samples and

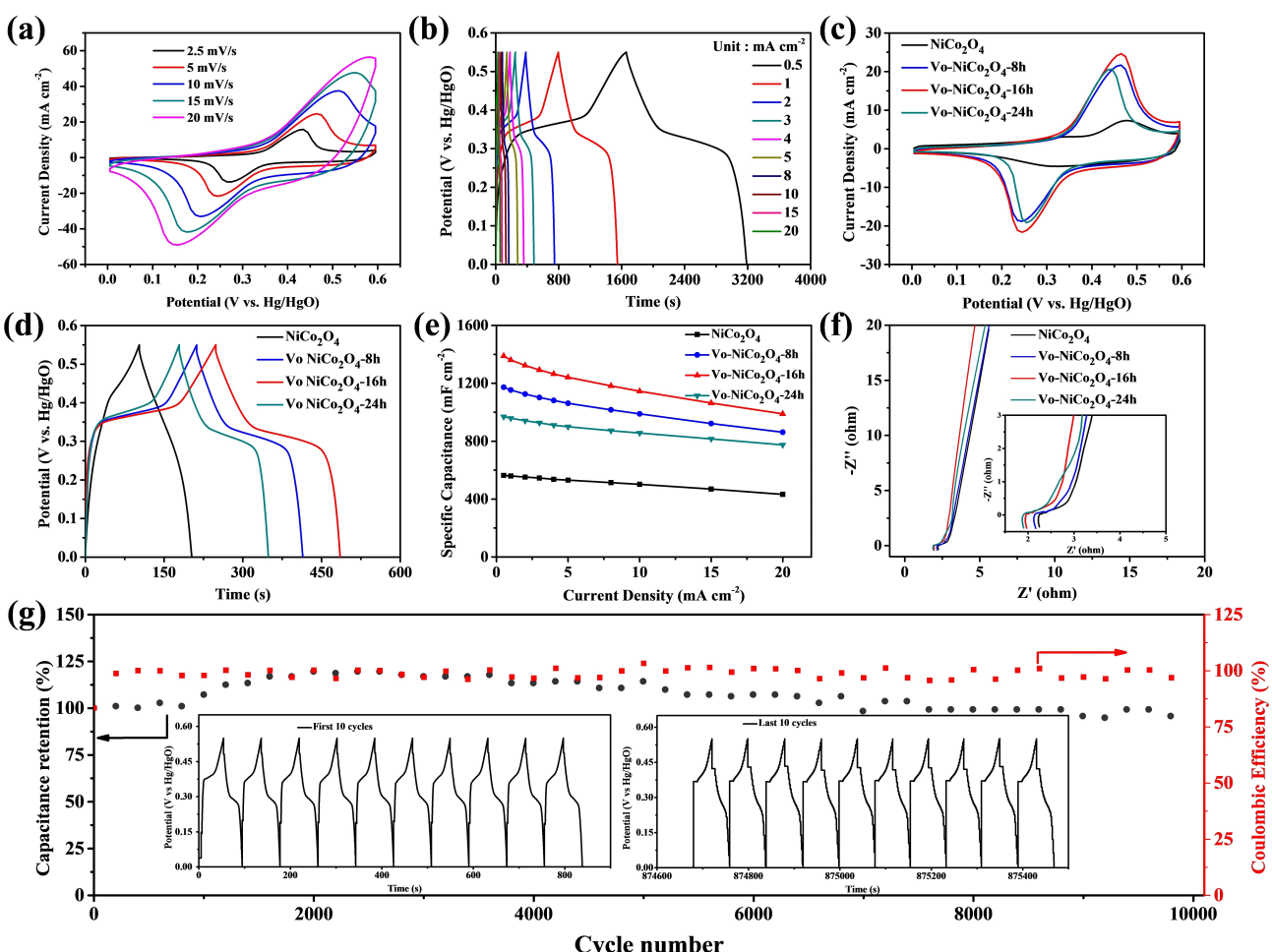


**Figure 4.** Electrochemical performance of investigated samples. a) CV curves and b) GCD curves of  $\text{Vo-NiCo}_2\text{O}_4@\text{CC-16h}$  measured at different scanning rates and different current densities, respectively; c) CV curves measured at  $5 \text{ mV s}^{-1}$ ; d) GCD curves recorded at  $3 \text{ mA cm}^{-2}$ ; e) areal capacitance changes as a function of current density and f) EIS Nyquist plots of  $\text{Vo-NiCo}_2\text{O}_4@\text{CC-xh}$  ( $x = 8, 16, 24$ ) and pristine  $\text{NiCo}_2\text{O}_4@\text{CC}$ ; g) cycling stability of  $\text{Vo-NiCo}_2\text{O}_4@\text{CC-16h}$  at  $10 \text{ mA cm}^{-2}$  for 10000 cycles. The insets (left and right) are the first 10 and the last 10 cycles of the charge/discharge curves of the electrode, respectively.

form more electrochemical reaction active sites as well as the increased surface area, which can all account for the high current density and the strong redox peak response of these  $\text{Vo-NiCo}_2\text{O}_4@\text{CC}$  samples.

The GCD curves of pristine  $\text{NiCo}_2\text{O}_4@\text{CC}$  and  $\text{Vo-NiCo}_2\text{O}_4@\text{CC}$  samples are presented in Figure 4(d). With the increase of solvothermal treatment time from 0 to 24 hours, both the energy storage capacity and the discharge time of the resulting samples increase remarkably. The  $\text{Vo-NiCo}_2\text{O}_4@\text{CC-16h}$  sample exhibits the longest discharge time. Actually, the discharge time of sample  $\text{Vo-NiCo}_2\text{O}_4@\text{CC-16h}$  is 2.5 times of pristine  $\text{NiCo}_2\text{O}_4@\text{CC}$ , further indicating larger energy storage capacitance of  $\text{Vo-NiCo}_2\text{O}_4@\text{CC-16h}$ . The large energy storage capacity and the long discharge time of sample  $\text{Vo-NiCo}_2\text{O}_4@\text{CC-16h}$  maybe ascribe to the formation of increased oxygen vacancies via solvothermal treatment in ethylene glycol alkaline solution but maintaining its structure integrity. These results further confirm that this mild solvothermal treatment in ethylene glycol alkaline solution is a readily effective approach to introduce defects such as oxygen vacancies into the electrode materials and enhance their electrochemical energy storage abilities.

To assess the rate performance, the areal capacitances of the pristine  $\text{NiCo}_2\text{O}_4@\text{CC}$  and  $\text{Vo-NiCo}_2\text{O}_4@\text{CC}$  samples calculated based on the discharge time of the GCD curves at different current densities are presented in Figure 4(e). Notably, the areal capacitance of  $\text{Vo-NiCo}_2\text{O}_4@\text{CC-16h}$  is remarkably high up to  $1389 \text{ mF cm}^{-2}$  at the current density of  $0.5 \text{ mA cm}^{-2}$ , which is much higher than and up to 2.5 times of that of the pristine  $\text{NiCo}_2\text{O}_4@\text{CC}$  ( $564 \text{ mF cm}^{-2}$ ) at the same current density. When the current density is increased by 40 times to  $20 \text{ mA cm}^{-2}$ , the sample  $\text{Vo-NiCo}_2\text{O}_4@\text{CC-16h}$  still exhibits a high specific capacitance of  $989 \text{ mF cm}^{-2}$ , which is still up to 2.3 times of that of pristine  $\text{NiCo}_2\text{O}_4@\text{CC}$  under the same conditions, indicating superior rate performance of the solvothermal treated samples. The rate performance values of the other two samples obtained under different solvothermal treatment time are between  $\text{Vo-NiCo}_2\text{O}_4@\text{CC-16h}$  and  $\text{NiCo}_2\text{O}_4@\text{CC}$ . Moreover, the gravimetric capacitance of the pristine  $\text{NiCo}_2\text{O}_4@\text{CC}$  and  $\text{Vo-NiCo}_2\text{O}_4@\text{CC}$  samples is given in Figure S7 and the change trends of the gravimetric capacitances of those samples are similar to that of their areal capacitances. It is worthwhile noting that among all the studied  $\text{Vo-NiCo}_2\text{O}_4@\text{CC}$  and  $\text{NiCo}_2\text{O}_4@\text{CC}$  samples,  $\text{Vo-NiCo}_2\text{O}_4@\text{CC-16h}$  exhibits the highest areal capacitance and gravimetric capacitance under the same current density, as well as the highest rate performance and specific capacitance.

Electrochemical impedance spectra (EIS) curves are obtained to assess the electrochemical performance of  $\text{Vo-NiCo}_2\text{O}_4@\text{CC-xh}$  and  $\text{NiCo}_2\text{O}_4@\text{CC}$ . From the Nyquist plot (Figure 4f), the equivalent series resistance ( $R_s$ ) can be acquired from the intercept of X axis at high frequency region, the  $R_s$  value of  $\text{Vo-NiCo}_2\text{O}_4@\text{CC-xh}$  are obviously lower than that of  $\text{NiCo}_2\text{O}_4@\text{CC}$ , indicating that introduction of oxygen vacancies can improve the electronic conductivity of solvothermal processed  $\text{Vo-NiCo}_2\text{O}_4@\text{CC-xh}$  samples.<sup>[20,46]</sup> The radius of the semicircular arc on the real axis stand for charge transfer

resistance ( $R_{ct}$ ). It can be distinctly seen that all the four samples display very small  $R_{ct}$ . The line shown in the low frequency region is almost vertical. And the slope of  $\text{Vo-NiCo}_2\text{O}_4@\text{CC-16h}$  is bigger, suggesting a lower diffusion resistance than that of  $\text{NiCo}_2\text{O}_4@\text{CC}$ . All above results clearly revealed the current mild solvothermal process method can effectively introduce oxygen vacancies and obviously increases the electronic conductivity, therefore leads to remarkable improved electrochemical performance of  $\text{Vo-NiCo}_2\text{O}_4@\text{CC-16h}$ . Moreover, cycling stability of  $\text{Vo-NiCo}_2\text{O}_4@\text{CC-16h}$  was evaluated to examine its long-term stability and coulombic efficiency. As shown in Figure 4(g), after 10000 consecutive charge and discharge cycles at  $10 \text{ mA cm}^{-2}$ , no obvious capacitance decrease is observed, and the  $\text{Vo-NiCo}_2\text{O}_4@\text{CC-16h}$  actually maintained 93.8% of its initial capacitance, indicating excellent electrochemical stability. The coulombic efficiency of this material is maintained at 100% without observable changes after 10000 cycles. In addition, the first and last 10 charge and discharge cycles of this samples further clearly show no observable decrease in the capacitance, suggesting excellent stability of this electrode material. The cycling performance of the pristine  $\text{NiCo}_2\text{O}_4@\text{CC}$  was also tested under the same conditions and the result is presented in Figure S8. After 10000 charge/discharge cycles running, the coulombic efficiency of this material is kept at 100% unchanged, but the capacitance retention of the pristine  $\text{NiCo}_2\text{O}_4@\text{CC}$  is only 61.5%, which is much lower than that of sample  $\text{Vo-NiCo}_2\text{O}_4@\text{CC-16h}$ , demonstrating the remarkably improvement of cycling stability of the solvothermal processed sample  $\text{Vo-NiCo}_2\text{O}_4@\text{CC-16h}$ .

To match with the  $\text{Vo-NiCo}_2\text{O}_4@\text{CC-16h}$  as cathode, an AC@CC anode was prepared. The CV curve of the AC@CC recorded at  $5 \text{ mV s}^{-1}$  shows almost rectangular shape (Figure 5a), indicating the typical electrical double-layer capacitance (EDLC) characteristic of carbon materials, and the CV curve of  $\text{Vo-NiCo}_2\text{O}_4@\text{CC-16h}$  at the same scanning rate was also shown in the same figure (Figure 5a). The detailed electrochemical performance of AC@CC single electrode acquired in a three-electrode system, was presented in Figure S9. The CV curves of AC@CC keep quasi-rectangular shape with little change at various scanning rates (Figure S9a), and the GCD curves of AC@CC steadily remain symmetric shape even the current density reached at  $20 \text{ mA cm}^{-2}$  (Figure S9b). Both the CV and GCD curves indicate the EDLC feature of AC@CC anode. Moreover, the AC@CC exhibits a specific capacitance of  $1177.6 \text{ mF cm}^{-2}$  at current density of  $2 \text{ mA cm}^{-2}$ , while this electrode maintains a rate performance of  $644 \text{ mF cm}^{-2}$  when the current density increased to  $20 \text{ mA cm}^{-2}$  (Figure S9c). The EIS result in Figure S9(d) indicates good conductivity of the AC@CC. The long-term cycling performance of the AC@CC is given in Figure S9e. Obviously, after 10000 cycles, the AC@CC electrode remains 92.8% of its initial capacitance value, indicating remarkable cycling stability of the active carbon.

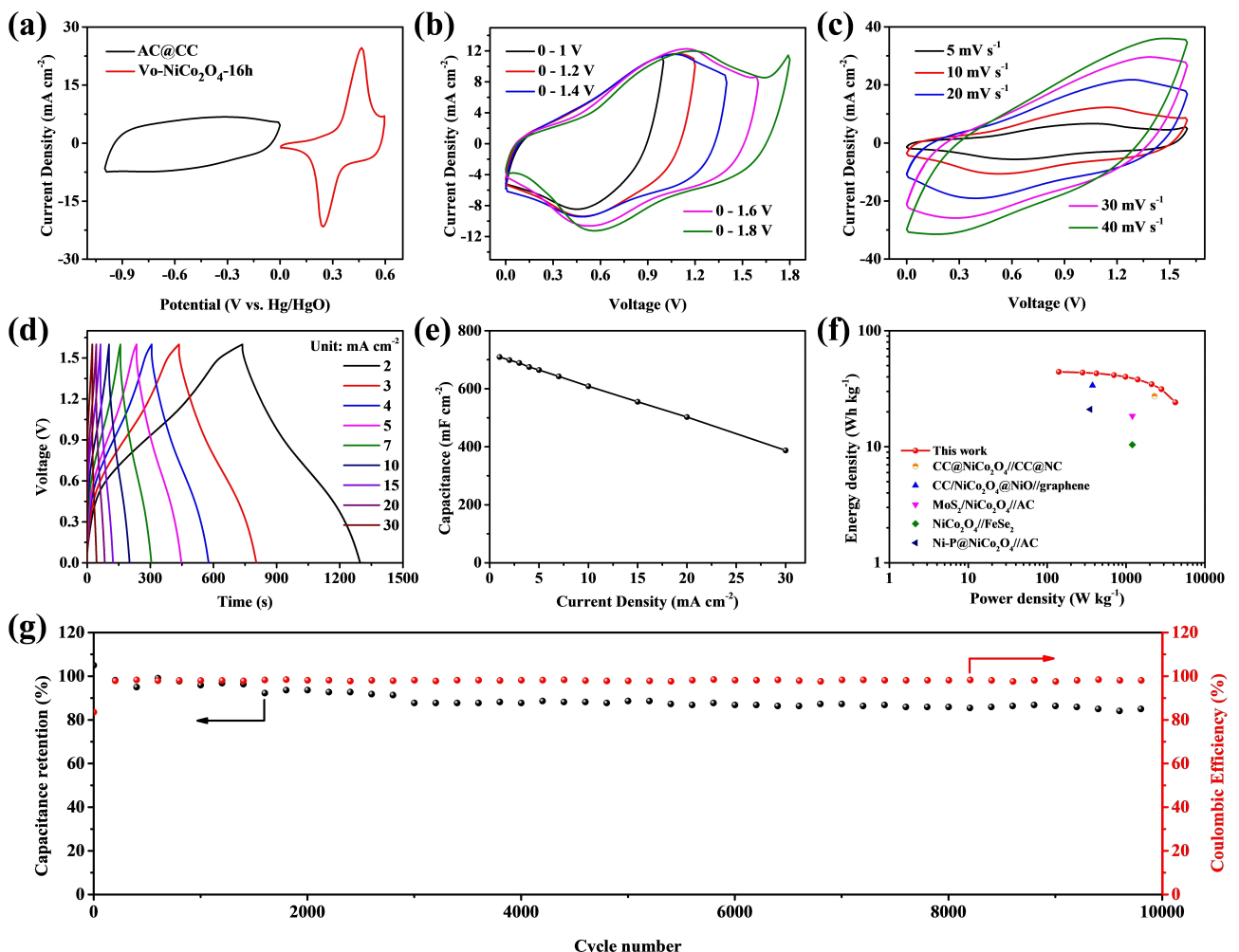


**Figure 5.** a) CV curves of the Vo-NiCo<sub>2</sub>O<sub>4</sub>@CC-16h and AC@CC electrode at 5 mV s<sup>-1</sup> in a three-electrode system; electrochemical b) CV curves at 10 mV s<sup>-1</sup> in different voltage windows range, c) CV curves under different scanning rates, d) GCD curves, e) rate performance, f) Ragone plots and g) cycling performance of the Vo-NiCo<sub>2</sub>O<sub>4</sub>@CC-16h//AC@CC aqueous asymmetric supercapacitor device.

### Asymmetric supercapacitor performance

To explore the potential application of the produced binder-free Vo-NiCo<sub>2</sub>O<sub>4</sub>@CC-16h electrode, an aqueous asymmetric supercapacitor (ASC) is assembled based on the Vo-NiCo<sub>2</sub>O<sub>4</sub>@CC-16h as cathode and AC@CC as anode. Firstly, the ASC device was measured at various voltage windows from 1.0 to 1.8 V to ascertain the optimal work window (Figure 5b). The CV curves maintain their initial shapes when the potential is up to 1.6 V. However, when the potential increased to 1.8 V, the CV curve turns to be gradually different from their original shapes due to the severe polarization caused by the oxygen evolution. Therefore, the optimized work potential of the ASC device is in the range of 0–1.6 V. The CV curves with various scanning rates from 5 to 50 mV s<sup>-1</sup> of the aqueous ASC are shown in Figure 5(c). It is obvious that the device can work steadily in the voltage window up to 1.6 V and the CV curves exhibit similar shape with redox peaks, indicating electrochemical double-layer capacitive and Faradic mechanism.<sup>[29]</sup> The GCD curves of this ASC device at different current densities

are presented in Figure 5(d) and the rate performance is given in Figure 5(e). The Vo-NiCo<sub>2</sub>O<sub>4</sub>@CC-16h//AC@CC device achieved a specific capacitance of 699 mF cm<sup>-2</sup> at a current density of 2 mA cm<sup>-2</sup>, and still retained 55.5% capacitance of its rate performance when the current density increased to 30 mA cm<sup>-2</sup>, revealing reasonably good rate performance of this assembled asymmetric supercapacitor. The energy density and power density of this Vo-NiCo<sub>2</sub>O<sub>4</sub>@CC-16h//AC@CC device and relevant data collected from literatures are listed and compared in the Ragone plot (Figure 5f). The as-prepared ASC device shows an excellent energy density of 43.6 Wh kg<sup>-1</sup> at power density of 281 W kg<sup>-1</sup> and it even retains an energy density of 24.2 Wh kg<sup>-1</sup> at power density of 4210.5 W kg<sup>-1</sup>. These values are much higher than other reported results in similar ASC system, such as CC@NiCo<sub>2</sub>O<sub>4</sub>//CC@NC (27.3 Wh kg<sup>-1</sup> at 2290 W kg<sup>-1</sup>),<sup>[27]</sup> CC/NiCo<sub>2</sub>O<sub>4</sub>@NiO//graphene (33.8 Wh kg<sup>-1</sup> at 375 W kg<sup>-1</sup>),<sup>[17]</sup> MoS<sub>2</sub>/NiCo<sub>2</sub>O<sub>4</sub>//AC (18.4 Wh kg<sup>-1</sup> at 1200.2 W kg<sup>-1</sup>),<sup>[21]</sup> NiCo<sub>2</sub>O<sub>4</sub>//FeSe<sub>2</sub> (10.4 Wh kg<sup>-1</sup> at 1200 W kg<sup>-1</sup>),<sup>[24]</sup> and Ni-P@NiCo<sub>2</sub>O<sub>4</sub>//AC (21 Wh kg<sup>-1</sup> at 350 W kg<sup>-1</sup>).<sup>[48]</sup> Moreover, the energy and power density

calculated by the area of this aqueous ASC device are presented in Figure S10, and it exhibits high energy density of  $0.25 \text{ mWh cm}^{-2}$  at the power density of  $0.8 \text{ mW cm}^{-2}$  and retains energy density of  $0.14 \text{ mWh cm}^{-2}$  at power density of  $24 \text{ mW cm}^{-2}$ . The long-term cycling stability of the ASC device is shown in Figure 5(g), and the device exhibits 85.5% capacitance retention after 10000-cycle operations with the coulombic efficiency close to 100%, indicating a remarkable cycling stability of the  $\text{Vo-NiCo}_2\text{O}_4@\text{CC-16h//AC@CC}$  device. In addition, the CV, GCD, EIS curves for this device were obtained after 10000-cycle operations as shown in Figure S11. Comparing the electrochemical performance of this aqueous  $\text{Vo-NiCo}_2\text{O}_4@\text{CC-16h//AC@CC}$  device before and after 10000 cycles running, it is clear that the discharge time turns to be slightly shortened after long term operation of the device, which reflects only a slight capacitance loss and good cycling stability of the assembled ASC device.

To demonstrate the practical application of the ASC, a quasi-solid-state ASC is assembled using  $\text{Vo-NiCo}_2\text{O}_4@\text{CC-16h}$  as cathode, AC@CC as anode and PVA/KOH gel as quasi-solid-state electrolyte. The CV curves in Figure 6(a) display excellent

capacitive behavior and stable operating voltage of the  $\text{Vo-NiCo}_2\text{O}_4@\text{CC-16h//AC@CC}$  device. Simultaneously, the GCD curves of the device displayed quasi-triangular shape under various current densities, further confirmed the capacitive characteristic of the quasi-solid state ASC device (Figure 6b). In addition, this device also possesses good rate performance as shown in Figure 6(c), and the specific capacitance of this  $\text{Vo-NiCo}_2\text{O}_4@\text{CC-16h//AC@CC}$  quasi-solid state ASC device varies from 434 to  $278 \text{ mF cm}^{-2}$  when the current density is changed from 2 to  $30 \text{ mA cm}^{-2}$ , suggesting a capacitance retention of 64.1%. A high energy density of  $27.1 \text{ Wh kg}^{-1}$  is achieved for the quasi-solid-state device at the power density of  $281 \text{ W kg}^{-1}$  (corresponding to the areal energy density of  $0.15 \text{ mWh cm}^{-2}$  at the power density of  $1.6 \text{ mW cm}^{-2}$ ). This quasi-solid state ASC device retains energy density of  $17.3 \text{ Wh kg}^{-1}$  at the power density of  $4210.5 \text{ W kg}^{-1}$  (corresponding to areal energy density of  $0.099 \text{ mWh cm}^{-2}$  at the power density of  $24 \text{ mW cm}^{-2}$ ), as presented in Figures 6(d) and S12(a). These results are much higher than those of similar systems reported in literature, such as Ni-Co oxide//AC ( $7.4 \text{ Wh kg}^{-1}$  at  $1902.9 \text{ W kg}^{-1}$ ),<sup>[49]</sup> NC@ $\text{Co}_3\text{O}_4$ //Co-NC@ $\text{Fe}_2\text{O}_3$  ( $8.8 \text{ Wh kg}^{-1}$  at  $3900 \text{ W kg}^{-1}$ ),<sup>[50]</sup> MoS<sub>2</sub>/

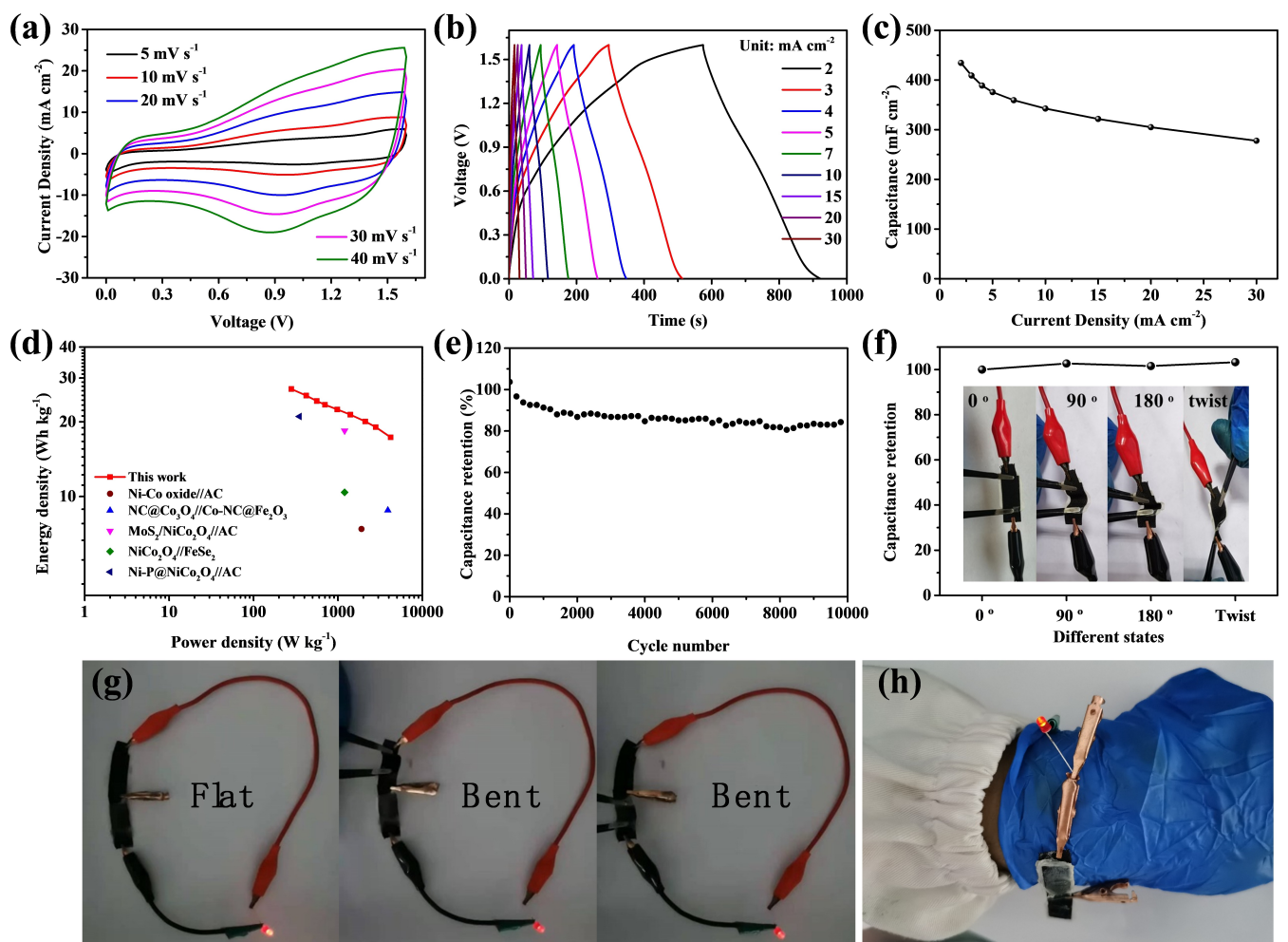


**Figure 6.** Electrochemical a) CV curves, b) GCD curves, c) rate performance, d) Ragone plot and e) cycling performance of the quasi-solid-state  $\text{Vo-NiCo}_2\text{O}_4@\text{CC-16h//AC@CC}$  ASC device. f) Capacitance retention of the quasi-solid-state ASC under different status (insets are optical photographs of the  $\text{Vo-NiCo}_2\text{O}_4@\text{CC-16h//AC@CC}$  device tested under various bending angles and twist status); g and h) Flexibility of the two quasi-solid-state ASC in series.

$\text{NiCo}_2\text{O}_4/\text{AC}$  ( $18.4 \text{ Wh kg}^{-1}$  at  $1200.2 \text{ W kg}^{-1}$ ),<sup>[21]</sup>  $\text{NiCo}_2\text{O}_4/\text{FeSe}_2$  ( $10.4 \text{ Wh kg}^{-1}$  at  $1200 \text{ W kg}^{-1}$ ),<sup>[24]</sup> and  $\text{Ni-P@NiCo}_2\text{O}_4/\text{AC}$  ( $21 \text{ Wh kg}^{-1}$  at  $350 \text{ W kg}^{-1}$ ).<sup>[48]</sup> The EIS result (Figure S12b) also indicates the fast charge transferring and ions diffusion properties of the device. The cycling performance of quasi-solid-state  $\text{Vo-NiCo}_2\text{O}_4@\text{CC-16h}/\text{AC@CC}$  supercapacitor is given in Figure 6(e). After 10000 cycles of running, this quasi-solid state ASC device maintained 84% of the initial capacitance, demonstrating a superior cycling stability. The mechanical flexibility of the assembled ASC device is of great importance parameter to meet the demand of flexible electronic applications. The GCD curves obtained under different status, such as bending, twisting are shown in Figure S12(c). As expected, the assembled quasi-solid-state ASC exhibits around 100% capacitance retention under different status including bending and twisting (Figure 6f), showing excellent flexibility and electrochemical stability of the ASC device. To demonstrate the practical application and flexibility more vividly, two devices connected in series are used to light up a red light-emitting diode (LED) under flat, bent status or even mounted on demonstrator's wrist, the brightness of the LED remains unchanged (Figure 6g and h), clearly demonstrating its promising potential to be used as an energy storage and power supply in wearable devices.

## Conclusion

In summary,  $\text{NiCo}_2\text{O}_4$  nanoneedle arrays that are in-situ grown on carbon cloth with significant increased oxygen vacancies introduced through a mild solvent thermal treatment method are prepared as a high-performance flexible cathode material for aqueous asymmetric supercapacitor. The solvothermal treated  $\text{Vo-NiCo}_2\text{O}_4$  with significant enhanced oxygen vacancies and increased surface area endow it excellent electrochemical energy storage performance. The areal capacitance of  $\text{Vo-NiCo}_2\text{O}_4@\text{CC}$  at  $0.5 \text{ mA cm}^{-2}$  reaches to  $1389 \text{ mF cm}^{-2}$ , which is 2.5 times to that of the pristine  $\text{NiCo}_2\text{O}_4@\text{CC}$  under the same conditions. Moreover, the  $\text{Vo-NiCo}_2\text{O}_4@\text{CC}$  possesses an excellent cycling stability with 93.8% capacitance retention after 10000 cycles running. In addition, the assembled  $\text{Vo-NiCo}_2\text{O}_4@\text{CC-16h}/\text{AC@CC}$  device achieves a good energy density of  $43.6 \text{ Wh kg}^{-1}$  at power density of  $281 \text{ W kg}^{-1}$  and shows good flexibility under different status. These results demonstrate that  $\text{Vo-NiCo}_2\text{O}_4@\text{CC}$  is an excellent flexible cathode material for supercapacitor and ethylene glycol solvent thermal treatment of alkaline solution is an effective approach to engineering oxygen vacancies and improve electrochemical performance of energy storage materials.

## Experimental Section

**Preparation of  $\text{NiCo}_2\text{O}_4@\text{CC}$ :** In a typical process,  $\text{Co}(\text{NO}_3)_2 \cdot 6\text{H}_2\text{O}$  (0.58 g),  $\text{Ni}(\text{NO}_3)_2 \cdot 6\text{H}_2\text{O}$  (0.29 g), and urea (0.3 g) were added into deionized (DI) water (20 mL) under stirring for 15 min, then transferred the mixture into a Teflon-lined stainless autoclave. A piece of clean carbon cloth (CC) was placed into the above

solution. After the autoclave was hydrothermal heated at  $120^\circ\text{C}$  for 4 h, the CC was taken out and rinsed with DI water, followed by drying at  $60^\circ\text{C}$ , and the obtained sample is named as  $\text{NiCo-LDH}@CC$ . Finally, the dried  $\text{NiCo-LDH}@CC$  was placed in a tube furnace and calcined in air at  $300^\circ\text{C}$  for 2 h with a heating ramp rate of  $2^\circ\text{C min}^{-1}$ . The product is designated as  $\text{NiCo}_2\text{O}_4@CC$ , and the  $\text{NiCo}_2\text{O}_4$  mass loading on the CC is about  $2.4 \text{ mg cm}^{-2}$ .

**Preparation of  $\text{Vo-NiCo}_2\text{O}_4@CC$ :** A piece of  $\text{NiCo}_2\text{O}_4@CC$  was immersed into a glycol solution (30 mL) containing 1.2 g NaOH, then transferred the mixture solution into a Teflon-lined stainless-steel autoclave and maintain it at  $120^\circ\text{C}$  for several hours. After cool to room temperature, the collected product was washed with ethanol several times and dried at  $60^\circ\text{C}$  overnight. Different solvothermal treatment time (8, 16, 24 h) was carried out to optimize the best treatment time and the resulting products are denoted as  $\text{Vo-NiCo}_2\text{O}_4@\text{CC-xh}$  ( $x=8, 16, 24$ ). Unless otherwise stated, the  $\text{Vo-NiCo}_2\text{O}_4@CC$  in this text is the sample prepared under the condition of 16 hours. To measure the textural properties of the samples, powder forms of  $\text{NiCo}_2\text{O}_4$  and  $\text{Vo-NiCo}_2\text{O}_4-xh$  were collected and measured as they were produced via the same procedures as  $\text{NiCo}_2\text{O}_4@CC$  and  $\text{Vo-NiCo}_2\text{O}_4-xh@CC$ .

**Fabrication of flexible quasi-solid state asymmetric supercapacitor:** The flexible quasi-solid state asymmetric supercapacitor (ASC) was fabricated by using  $\text{Vo-NiCo}_2\text{O}_4@\text{CC-16h}$  as cathode, active carbon on CC (AC@CC) as anode, and PVA-KOH gel as electrolyte. The anode electrode was made by mixing the active carbon with acetylene black and PVDF (polyvinylidene fluoride) with a weight ratio of 8:1:1 in moderate amount of NMP (N-methyl-2-pyrrolidone), casting the mixture onto a piece of carbon cloth, and dried in an oven at  $60^\circ\text{C}$ . To assemble a quasi-solid state supercapacitor device, typically, 2.0 g PVA firstly added into 10 mL DI water, and heated at  $90^\circ\text{C}$  for 2 h. Then 10 mL 4 M KOH solution was added into above solution and stirred at  $90^\circ\text{C}$  for another 2 h. Subsequently,  $\text{NiCo}_2\text{O}_4@\text{CC-16h}$  and AC@CC were dipped into and fully immersed in the PVA-KOH gel. Followed by the assembling of  $\text{NiCo}_2\text{O}_4@\text{CC-16h}$  and AC@CC face to face with a separator located between them, the assembled device was finally left in ambient conditions for several hours to evaporate the excess water before test.

**Materials characterization:** The materials were characterized by XRD (Bruker D8 Advanced, 40 kV and 40 mA), field emission scanning electron microscopy (FESEM, FEI Verios G4, 20 kV), transmission electron microscopy (TEM, FEI Talos F200X, 200 kV). X-ray photoelectron spectroscopy (XPS) were collected on a PHI5400 equipment. To obtain the specific area of electrode materials,  $\text{N}_2$  gas adsorptions were measured at  $-196^\circ\text{C}$  on Quantachrome Autosorb iQ, the samples were outgassed at  $200^\circ\text{C}$  for 10 h before testing. Brunauer-Emmett-Teller (BET) method was used to calculate the surface area of the samples, based on the adsorption data in the partial pressure ( $P/P_0$ ) range of 0.02–0.22 and density functional theory (DFT) method were adopted to measure the pore size distribution. Electron paramagnetic resonance (EPR) were measured on an EPR spectrometer (Bruker-A300).

**Electrochemical measurements:** The electrochemical performances of produced materials were evaluated on an electrochemical workstation (CHI 760E) by a three-electrode configuration in 1 M KOH aqueous electrolyte, with Pt foil as the counter electrode and  $\text{Hg/HgO}$  as the reference electrode.  $\text{NiCo}_2\text{O}_4@CC$ ,  $\text{Vo-NiCo}_2\text{O}_4@\text{CC-xh}$  and AC@CC (both  $1.0 \text{ cm} \times 1.0 \text{ cm}$ ) were used directly as the working electrode. The data of cyclic voltammetry (CV), galvanostatic charge-discharge (GCD) measurements and electrochemical impedance spectra (EIS, performed at the frequency from 0.01 to 100 kHz with potential amplitude of 0.5 V) were also collected on the electrochemical workstation. The two-electrode system was

tested in 1 M KOH aqueous electrolyte and  $\text{Vo-NiCo}_2\text{O}_4@\text{CC}$ -16h and AC@CC were used as cathode and anode respectively. The cycle stability performance was studied using a Neware battery testing system.

## Acknowledgments

The authors thank the financial supports by National Natural Science Foundation of China (21571055, U20A20122, 22072038), and Applied Basic Frontier Project of Wuhan Science and Technology Bureau (2019010701011415). The authors also thank the Analytical & Testing Center of Northwestern Polytechnical University for TEM analysis.

## Conflict of Interest

The authors declare no conflict of interest.

## Data Availability Statement

The data that support the findings of this study are available from the corresponding author upon reasonable request.

**Keywords:** asymmetric supercapacitor • flexible energy storage •  $\text{NiCo}_2\text{O}_4$  nanoarrays • oxygen vacancies

- [1] S. Fleischmann, J. B. Mitchell, R. Wang, C. Zhan, D. E. Jiang, V. Presser, V. Augustyn, *Chem. Rev.* **2020**, *120*, 6738–6782.
- [2] C. Choi, D. S. Ashby, D. M. Butts, R. H. DeBlock, Q. Wei, J. Lau, B. Dunn, *Nat. Rev. Mater.* **2019**, *5*, 5–19.
- [3] E. Pomerantseva, F. Bonaccorso, X. Feng, Y. Cui, Y. Gogotsi, *Science* **2019**, *366*, 969.
- [4] Z. Liu, F. Mo, H. Li, M. Zhu, Z. Wang, G. Liang, C. Zhi, *Small Methods* **2018**, *2*, 1800124.
- [5] H. Li, Z. Tang, Z. Liu, C. Zhi, *Joule* **2019**, *3*, 613–619.
- [6] J. Lee, B. Llerena Zambrano, J. Woo, K. Yoon, T. Lee, *Adv. Mater.* **2019**, *33*, e1902532.
- [7] P. Simon, Y. Gogotsi, *Nat. Mater.* **2020**, *19*, 1151–1163.
- [8] J. Shang, Q. Huang, L. Wang, Y. Yang, P. Li, Z. Zheng, *Adv. Mater.* **2020**, *32*, e1907088.
- [9] D. Chao, S.-Z. Qiao, *Joule* **2020**, *4*, 1846–1851.
- [10] B. Yao, S. Chandrasekaran, J. Zhang, W. Xiao, F. Qian, C. Zhu, E. B. Duoss, C. M. Spadaccini, M. A. Worsley, Y. Li, *Joule* **2019**, *3*, 459–470.
- [11] Y. Zeng, Y. Han, Y. Zhao, Y. Zeng, M. Yu, Y. Liu, H. Tang, Y. Tong, X. Lu, *Adv. Energy Mater.* **2015**, *5*, 1402176.
- [12] P. Gao, P. Metz, T. Hey, Y. Gong, D. Liu, D. D. Edwards, J. Y. Howe, R. Huang, S. T. Misture, *Nat. Commun.* **2017**, *8*, 14559.
- [13] S. V. Talande, A. Bakandritos, P. Jakubec, O. Malina, R. Zbořil, J. Tuček, *Adv. Funct. Mater.* **2019**, *29*, 1906998.
- [14] N. Yu, H. Yin, W. Zhang, Y. Liu, Z. Tang, M.-Q. Zhu, *Adv. Energy Mater.* **2016**, *6*, 1501458.
- [15] Y. Yan, J. Liu, K. Huang, J. Qi, L. Qiao, X. Zheng, W. Cai, *J. Mater. Chem. A* **2021**. doi: 10.1039/d1ta07972g.
- [16] Y. Ha, L. Shi, X. Yan, Z. Chen, Y. Li, W. Xu, R. Wu, *ACS Appl. Mater. Interfaces* **2019**, *11*, 45546–45553.
- [17] Y. Ouyang, R. Huang, X. Xia, H. Ye, X. Jiao, L. Wang, W. Lei, Q. Hao, *Chem. Eng. J.* **2019**, *355*, 416–427.
- [18] L. Shen, Q. Che, H. Li, X. Zhang, *Adv. Funct. Mater.* **2014**, *24*, 2630–2637.
- [19] J. Du, Q. Cao, X. Tang, X. Xu, X. Long, J. Ding, C. Guan, W. Huang, *Chem. Eng. J.* **2021**, *416*, 127885.
- [20] D. Yan, W. Wang, X. Luo, C. Chen, Y. Zeng, Z. Zhu, *Chem. Eng. J.* **2018**, *334*, 864–872.
- [21] S. Wen, Y. Liu, F. Zhu, R. Shao, W. Xu, *Appl. Surf. Sci.* **2018**, *428*, 616–622.
- [22] Z. Cai, Y. Bi, E. Hu, W. Liu, N. Dwarica, Y. Tian, X. Li, Y. Kuang, Y. Li, X.-Q. Yang, H. Wang, X. Sun, *Adv. Energy Mater.* **2018**, *8*, 1701694.
- [23] J. Qi, Y. Yan, Y. Cai, J. Cao, J. Feng, *Adv. Funct. Mater.* **2020**, *31*, 2006030.
- [24] C. Ji, F. Liu, L. Xu, S. Yang, *J. Mater. Chem. A* **2017**, *5*, 5568–5576.
- [25] H. Zhang, D. Xiao, Q. Li, Y. Ma, S. Yuan, L. Xie, C. Chen, C. Lu, *J. Energy Chem.* **2018**, *27*, 195–202.
- [26] X. Yin, H. Li, L. Han, J. Meng, J. Lu, Q. Song, *Small* **2021**, *17*, e2008056.
- [27] C. Guan, X. Liu, W. Ren, X. Li, C. Cheng, J. Wang, *Adv. Energy Mater.* **2017**, *7*, 1602391.
- [28] J. Yang, X. Xiao, P. Chen, K. Zhu, K. Cheng, K. Ye, G. Wang, D. Cao, J. Yan, *Nano Energy* **2019**, *58*, 455–465.
- [29] Y. Zhang, Y. Hu, Z. Wang, T. Lin, X. Zhu, B. Luo, H. Hu, W. Xing, Z. Yan, L. Wang, *Adv. Funct. Mater.* **2020**, *30*, 2004172.
- [30] Z. Li, Y. Ren, L. Mo, C. Liu, K. Hsu, Y. Ding, X. Zhang, X. Li, L. Hu, D. Ji, G. Cao, *ACS Nano* **2020**, *14*, 5581–5589.
- [31] S. Sun, T. Zhai, C. Liang, S. V. Savilov, H. Xia, *Nano Energy* **2018**, *45*, 390–397.
- [32] Q. Ni, R. Dong, Y. Bai, Z. Wang, H. Ren, S. Sean, F. Wu, H. Xu, C. Wu, *Energy Storage Mater.* **2020**, *25*, 903–911.
- [33] M. Li, Q. Zhou, C. Ren, N. Shen, Q. Chen, J. Zhao, C. Guo, L. Zhang, J. Li, *Nanoscale* **2019**, *11*, 22550–22558.
- [34] M. Liang, M. Zhao, H. Wang, J. Shen, X. Song, *J. Mater. Chem. A* **2018**, *6*, 2482–2493.
- [35] C. He, B. Han, S. Han, Q. Xu, Z. Liang, J. Xu, M. Ye, X.-Y. Liu, J. Xu, *J. Mater. Chem. A* **2019**, *7*, 26884–26892.
- [36] Y. Wang, T. Zhou, K. Jiang, P. Da, Z. Peng, J. Tang, B. Kong, W.-B. Cai, Z. Yang, G. Zheng, *Adv. Energy Mater.* **2014**, *4*, 1400696.
- [37] L. Liao, Q. Zhang, Z. Su, Z. Zhao, Y. Wang, Y. Li, X. Lu, D. Wei, G. Feng, Q. Yu, X. Cai, J. Zhao, Z. Ren, H. Fang, F. Robles-Hernandez, S. Baldelli, J. Bao, *Nat. Nanotechnol.* **2014**, *9*, 69–73.
- [38] H. Tüysüz, Y. Liu, C. Weidenthaler, F. Schüth, *J. Am. Chem. Soc.* **2008**, *130*, 14108–14110.
- [39] C. Zhang, X. Cai, Y. Qian, H. Jiang, L. Zhou, B. Li, L. Lai, Z. Shen, W. Huang, *Adv. Sci.* **2018**, *5*, 1700375.
- [40] C. Xu, J. Liao, C. Yang, R. Wang, D. Wu, P. Zou, Z. Lin, B. Li, F. Kang, C.-P. Wong, *Nano Energy* **2016**, *30*, 900–908.
- [41] Y. Yan, J. Lin, J. Cao, S. Guo, X. Zheng, J. Feng, J. Qi, *J. Mater. Chem. A* **2019**, *7*, 24486–24492.
- [42] J. Bao, X. Zhang, B. Fan, J. Zhang, M. Zhou, W. Yang, X. Hu, H. Wang, B. Pan, Y. Xie, *Angew. Chem. Int. Ed.* **2015**, *54*, 7399–7404.
- [43] J. Yin, Y. Li, F. Lv, M. Lu, K. Sun, W. Wang, L. Wang, F. Cheng, Y. Li, P. Xi, S. Guo, *Adv. Mater.* **2017**, *29*, 1704681.
- [44] Q. Tan, X. Li, B. Zhang, X. Chen, Y. Tian, H. Wan, L. Zhang, L. Miao, C. Wang, Y. Gan, J. Jiang, Y. Wang, H. Wang, *Adv. Energy Mater.* **2020**, *10*, 2001050.
- [45] Q. Wang, Y. Luo, R. Hou, S. Zaman, K. Qi, H. Liu, H. S. Park, B. Y. Xia, *Adv. Mater.* **2019**, *31*, e1905744.
- [46] J. Zhao, Z. Li, X. Yuan, Z. Yang, M. Zhang, A. Meng, Q. Li, *Adv. Energy Mater.* **2018**, *8*, 1702787.
- [47] D. Cai, J. Du, C. Zhu, Q. Cao, L. Huang, J. Wu, D. Zhou, Q. Xia, T. Chen, C. Guan, Y. Xia, *ACS Appl. Energ. Mater.* **2020**, *3*, 12162–12171.
- [48] X. Li, R. Ding, L. Yi, W. Shi, Q. Xu, E. Liu, *Electrochim. Acta* **2016**, *222*, 1169–1175.
- [49] C. Tang, Z. Tang, H. Gong, *J. Electrochem. Soc.* **2012**, *159*, A651–A656.
- [50] C. Zhu, C. Guan, D. Cai, T. Chen, Y. Wang, J. Du, J. Wu, X. Xu, H. Yu, W. Huang, *Batteries & Supercaps* **2020**, *3*, 93–100.

Manuscript received: November 14, 2021

Revised manuscript received: December 2, 2021

Version of record online: December 18, 2021